Mechanical loss in bulk materials

R. Nawrodt[1], D. Heinert[1], G. Hofmann[1], P. Murray[2], C. Schwarz[1]
on behalf of the ELiTES WP2 members

[1] Friedrich-Schiller-Universität Jena, Institut für Festkörperphysik, Helmholtzweg 5, D-07743 Jena, Germany.
[2] SUPA, School of Physics and Astronomy, Institute for Gravitational Research, University of Glasgow, Glasgow G12 8QQ, United Kingdom

ET-0002A-13

28/02/2013

ELiTES is a IRSES-Marie Curie initiative , GA 295153.

Contents

1 Introduction **3**

2 Crystal growing techniques **4**
2.1 Growing from the gas phase 4
2.2 Hydrothermal synthesis of crystals 5
2.3 Crystal growth from the melt 6
2.3.1 Kyropoulos and Nacken method 6
2.3.2 Bridgman and Stockbarger method 7
2.3.3 Czochralski method 7
2.3.4 Heat exchange method 9
2.3.5 Float zone method 10
2.4 Verneuil method 11
2.5 Others 11
2.6 Zone refining technique 12

3 Mechanical loss and its measurement **14**
3.1 Anelastic behavior of solids 14
3.2 Experimental scheme of mechanical loss measurements 16
3.3 Numerical calculation of mechanical mode shapes 18

4 Mechanical loss mechanisms in solids **20**
4.1 Overview 20
4.2 Thermo-elastic damping 20
4.3 Phonon-Phonon damping 23
4.4 Electron-Phonon damping 26
4.5 Surface related damping 29
4.6 Point-defect induced damping mechanisms 30

1 Introduction

Thermal noise of the optical components can be a sensitivity limiting noise source in current and future gravitational wave detectors [1–4]. One important noise contribution - Brownian thermal noise - is directly related to the intrinsic mechanical loss ϕ of the material [5, 6].

This document summarises the different intrinsic sources of mechanical dissipation in bulk solids focusing on crystalline samples that are of particular interest for future gravitational wave detectors operating at cryogenic temperatures.

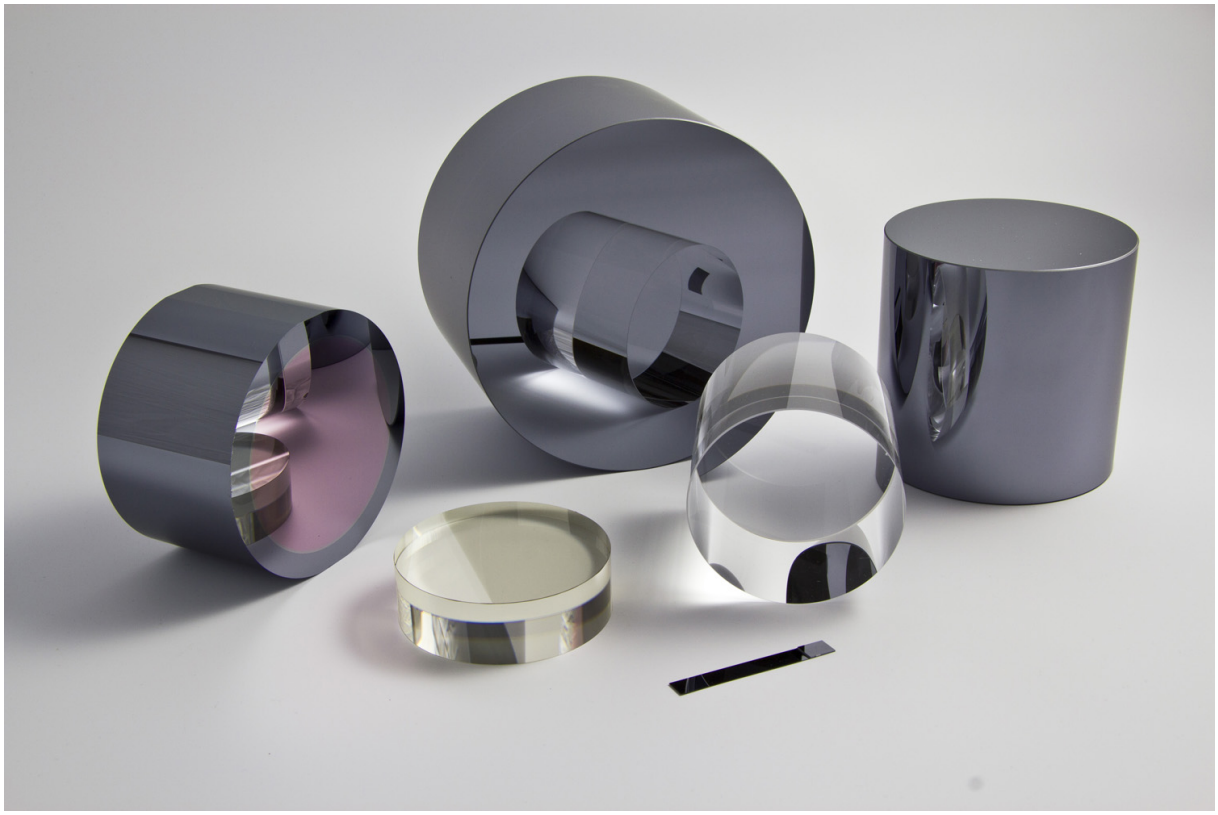

2 Crystal growing techniques

The following chapter will summarise the main crystal growing techniques that can be used to produce high quality crystalline bulk samples. Different techniques are available producing different qualities of single crystals. A historical overview of the development of crystal growing techniques can be found in [7,8]. Further details on crystal growth can be found in different text books, e.g. [9,10].

2.1 Growing from the gas phase

The first possibility is to grow the crystal from the gas phase. The material gets evaporated by heating or is directly formed from a gaseous phase. Typically, only a small amount of the material is available in gas phase in reactors of moderate sizes. Thus, a continuous flow of new reactants is needed in order to grow large crystals. Two general principles are used:

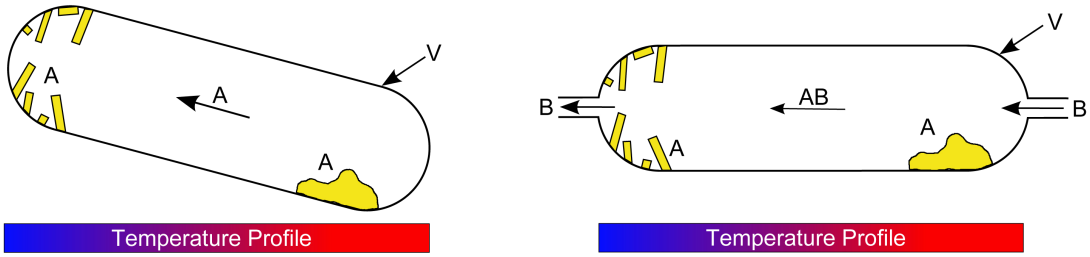

(a) (b)

Figure 2.1: Crystal growth from the gas phase using (a) a closed and (b) an open method.

Firstly, we consider the closed principle as shown in fig. 2.1(a). Here all raw material - which is typically polycrystalline - is placed into a sealed reactor. The reactor is heated in a two zone oven providing a higher temperature at the polycrystalline material and a colder zone where the single crystalline material should be grown. By means of electrical heating the raw material gets continuously evaporated and it condenses in the colder zone forming single crystalline pieces. In order to grow a single crystal it is beneficial to introduce a seed crystal before starting the growing process. Careful adjusting of the heater temperature allows a regime where the crystal growth only occurs at the seed crystal and the formation of new seeds is prevented. This is based on the fact that the optimum temperature to form seed crystals and to grow single crystalline materials are well seperated. Without the seed crystal random formation of seed crystals and an uncontrolled growth will start that leads to small crystals with dimensions between 3 and 20 mm. This method is mainly

used to grow smaller anorganic crystals like ZnTe, CdS, etc. An intermediate transport material can be used to bring the reactants to the growing phase (see fig. 2.1(b)). This method is often used when the raw material cannot be evaporated without decomposition. Examples are ZnS or GaP where iodine and Fe_2O_3 is used to temporary react with the raw material making it transportable in the gas phase. The chemical reaction is reversed at the growing site by thermal energy.

The second method is the open principle (see fig. 2.1(b)) where an inert process gas (e.g. nitrogen, argon or others) is used to assist the transport. Additionally, a chemical reaction inside the gas phase can be used to produce the material for the crystal growth. An important example is the epitaxial growth of silicon on silicon wafers from the gas phase. This gas phase contains hydrogen that transports silicon(IV) chloride to the silicon wafers that are heated. Here the chemical reaction forms silicon which grows epitaxially on the wafers leaving hydrochloric gas behind which is removed by means of a gas flow. These methods are called CVD (chemical vapor deposition) and play an important role in microelectronics today.

2.2 Hydrothermal synthesis of crystals

Hydrothermal growth of single crystals plays an important role in growing material for electronical and optical applications. Details of the method can be found e.g. in [11]. Water heated above the triple point can dissolve unusual amounts of typically unsolvable solids such as SiO_2 which makes it interesting for the growth of crystalline quartz. Overheated water at 400 °C is pressurized in a reactor to about 4000 atmospheres. SiO_2 gets dissolved until saturation adding sodium carbonate or hydroxide to assist the dissolving process. Seed crystals being cut from natural quartz are put into the reactor. The whole mixture is kept for several weeks. An epitaxial growth starts at the seed crystals forming large single crystals of quartz (see fig. 2.2(b)).

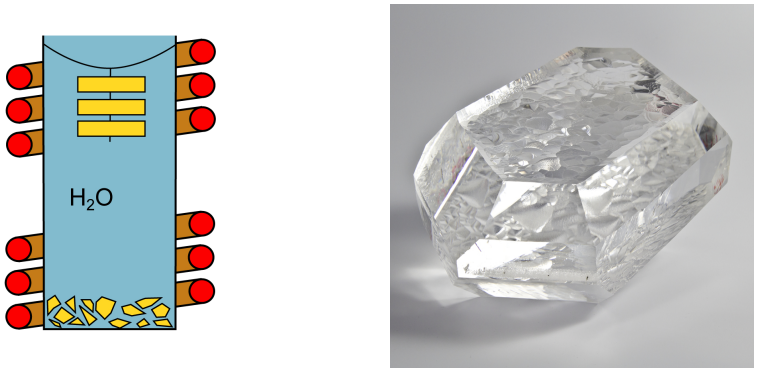

(a) (b)

Figure 2.2: (a) Hydrothermal growth of a crystal. Raw material gets dissolved in water under large pressured and high temperatures. Epitaxial growth starts at the seed crystals forming large single crystals. (b) Large quartz single crystal produced by the hydrothermal crystal growth technique (29 cm × 17 cm × 11 cm).

High quality single crystal quartz is grown using this method. These crystals are used to produce time keeping components (e.g. electronical quartzes), high-frequency filters or optical elements (e.g. waveplates). Besides its high optical and electronical quality, the added alkaline components, however, get also introduced into the quartz crystal causing point defects to occur. A sketch of the unperturbed quartz lattice and the geometry of the alkali defect is presented in fig. 2.3. As discussed in section 4.6 these point defects can be the origin of low temperature dissipation peaks.

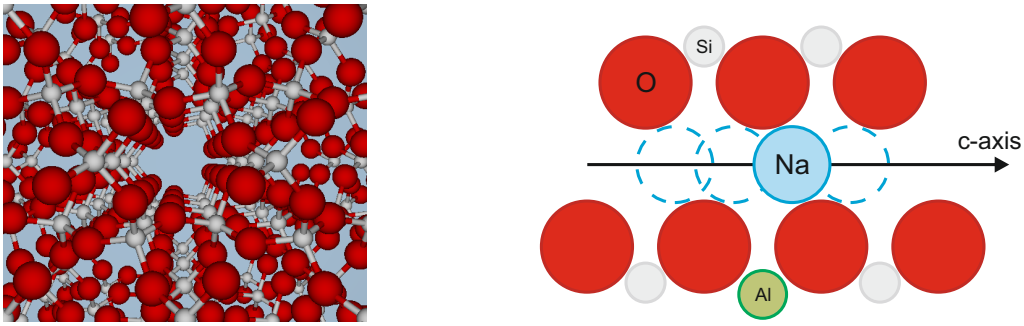

(a) (b)

Figure 2.3: (a) Crystal lattice structure of α-quartz. A view along the crystalline c-axis is shown. Oxygen atoms are colored in red and silicon atoms in grey. Note the channel formed by oxygen atoms in the mid of the picture. The sodium defect is illustrated in (b). Here a silicon atom is substituted by an aluminum atom. Due to the charge compensation sodium or another alkali atom enters the lattice. This atom experiences different equilibrium positions moving within the channel along the c-axis.

2.3 Crystal growth from the melt

Most of the industrial methods to grow large single crystals are based on the liquid-solid phase transition. Different methods exist in order to crystallise material from the liquid phase. By carefully choosing the temperature and crystallisation parameters it is possible to crystallise the full melt without producing new seed crystals, twins, grain boundaries or other defects.

2.3.1 Kyropoulos and Nacken method

The simplest crystallisation from the melt is to add a seed crystal to it and then cool the melt [12]. During cooling the melt will transfer into the solid state crystallising at the seed crystal. Latent heat from the phase transition liquid-solid heats the material which causes inhomogeneous recrystallisation. Great care needs to be taken in order to extract the heat. The quality of the single crystals produced by this method is rather low. They contain defects in the crystal lattice as well as stress in the crystal.

2.3.2 Bridgman and Stockbarger method

The methods developed by Bridgman and Stockbarger use a seed crystal at the lower end of a sealed reactor that contains the raw material. This reactor, also called ampoule, is moved through a vertical oven that provides a temperature gradient. The interface between liquid and crystallised phase becomes thus better defined. The crystal quality is much better.

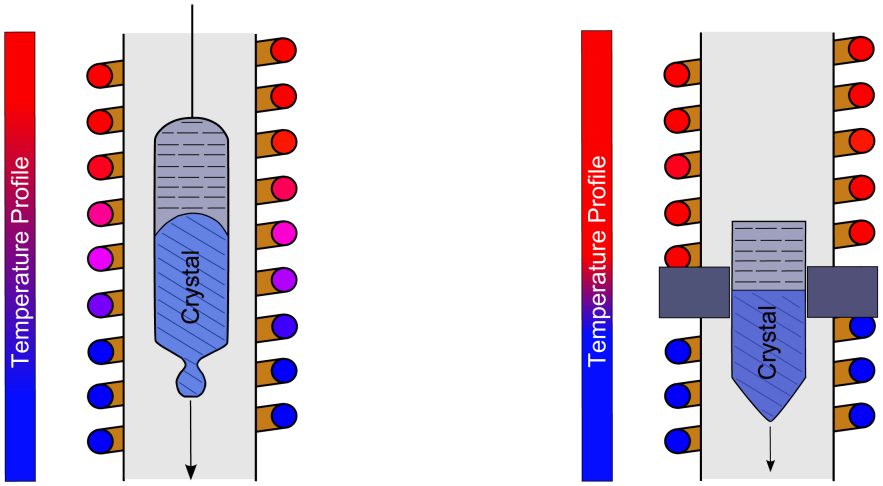

(a) (b)

Figure 2.4: Crystal growth after Bridgman (a) and Stockbarger (b). The Stockbarger method uses a metal ring to seperate different zones in the oven to provide a thermal gradient for the crystallisation.

The Bridgman-Stockbarger-Method is used to grow for example gallium arsenide single crystals. However, the size of the crystals is rather limited.

2.3.3 Czochralski method

The Czochralski method was invented by Jan Czochralski in 1916 and published in 1918 [13]. The Czochralski method is currently the most widely used method to grow semiconductor single crystals (mainly silicon) for electronical applications. The raw material (e.g. high purity poly-crystalline silicon) is melted in a crucible which is typically made of silica due to the requirements in temperature. A seed crystal is put into the melt and slowly pulled out again with a rate of mm/min (see fig. 2.5). A single crystal forms and can be grown to large sizes. The pulling rate determines the size of the crystal. Large crystals up to 300 mm are currently standard in the wafer production for semiconductor industry. In the experimental phase crystal growth up to 450 mm in diameter was shown. Larger sample diameters are under investigation for the semiconductor industry in order to reduce the price for electronic devices. A critical parameter in growing crystals by means of this method is the removal of the solidification heat. This heat is created at the interface between the liquid and the solid phase and needs to be removed carefully.

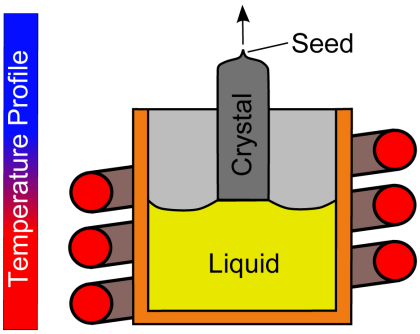

Figure 2.5: Czochralski method for growing large single crystals. A seed crystal is dipped into the melt and then slowing pulled out. At the interface liquid-solid a single crystal growth starts. The crystal diameter can be controlled by the pulling speed.

Additionally, the temperature inside the melt needs to be carefully kept constant. Magnetically assisted growing is used to support the homogeneity of the temperature profile in the melt. This method is called magnetically assisted Czochralski growth.

The melt is heated inside a silica bowle that is placed inside a graphite cruicable. This cruicable stiffenes the silica bowle as it starts deforming at the temperatures needed for the crystal growth (typically slightly above the melting temperature of silicon which is 1414 degrees Celcius). The graphite crucible can also be used for electrical heating of the system.

The crystal growth takes several hours in which the melt is able to react with the silica boat forming silicon monoxide. This material is transfered via convection or diffusion to both the interface melt – gas and melt – solid. At the interface melt – gas it evaporates and gets removed by a gas flow of noble gas (typically argon). However, parts of the chemically dissolved oxygen gets transfered to the interface liquid – solid and gets into the single crystal forming an impurity. In electronical applications oxygen concentrations of about $5...7 \times 10^{17}\,\mathrm{cm}^{-3}$ are preferred [14]. Thus, only 1% of the dissolved oxygen should finally enter the single crystal and sets strong limits to the operational parameters of the growing process.

Different defects exist in silicon. They can be divided into intrinsic defects (that are created by the silicon itself) and extrinsic defects that include impurity materials such as oxygen. The number of defects is strongly temperature dependent. Between 700 and 1000 °C there can be between 10^{15} and 10^{17} voids per cm^{-3} in pure silicon [15].

As a natural extrinsic defect oxygen plays and inportant role. Oxygen occupies interstitial places in silicon between two silicon atoms forming an electrically non-active defect. The exact structure of this defect is still under discussion. One of the possible structures is given in fig. 2.6 [15, 16], however, also linear defect geometries are under consideration [18, 19]. It is also under consideration for defect induced mechanical losses of silicon [17, 20].

Due to the long exposure time of the silicon to the silica bowle during crystal growth the saturation concentration of oxygen in silicon is quickly reached. Liquid silicon can dissolve oxygen in a concentration up to $10^{19}\,\mathrm{cm}^{-3}$. Reducing the temperature slightly

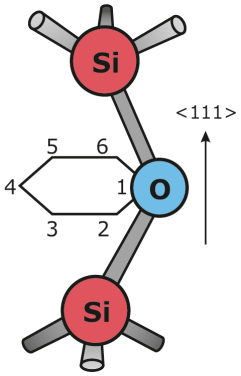

Figure 2.6: Interstitially bound oxygen in silicon. The oxygen atom occupies a place between two silicon atoms [15–17].

below the melting point only $2 \times 10^{18}\,\mathrm{cm}^{-3}$ oxygen atoms can be stable in silicon and thus oxygen starts to form precipitations if the melt was saturated with oxygen.. The dynamics of the oxygen-based defects in silicon are widely discussed in literature forming the important task of impurity engineering for the semiconductor industry.

The foreseen step to a production of 450 mm as well as 675 mm diameter single crystals is under discussion [14].

2.3.4 Heat exchange method

The heat exchange method (HEM) was developed by Schmid and Viechnicki in 1970 [21, 22]. It is an advanced gradient freeze technique. The raw material gets heated in a crucible. A seed crystal is placed at the bottom of the melt inside the crucible and is cooled from the back side by means of an heat exchanger (see fig. 2.7).

The heat exchanger is cooled by means of helium gas which provides a good thermal

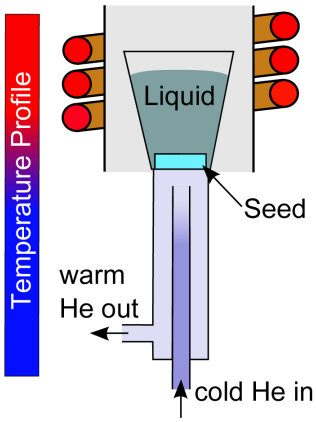

Figure 2.7: Heat Exchange Method used to grow large pieces of sapphire. A seed crystal is placed into the melt. This crystal is cooled from the back side by means of a heat exchanger. This allows the precise control of the crystal growing parameters.

conductivity. The temperature of the seed crystal is thus controlled and a desired temperature gradient within the melt/crystal can be obtained. This allows the growth of large single crystals with an excellent quality. It is currently the best method to grow large sapphire single crystals [23] and can be used as well to grow other crystals such as silicon [24].

2.3.5 Float zone method

The float zone method transforms the polycrystalline raw material into a high-purity single crystal. The raw material already has the shape of a cylinder and gets heated in a small zone. Heating can be done using inductive methods. At one end a seed crystal is added to start the crystallisation. Moving the liquid zone slowly through the raw material crystallises it (see fig. 2.8). This crucible-free method allows the fabrication of high purity single-crystals.

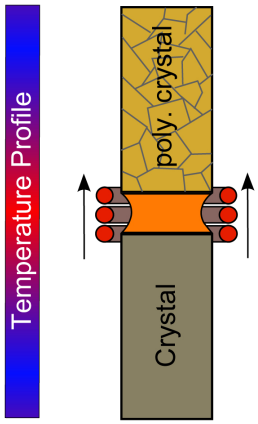

Figure 2.8: Float zone crystal growing technique. The upper part of the sample contains the raw material which can be monocrystalline or polycrystalline. The lower part of the sample is the high purity single crystal produced by the float zone method.

Subsequent steps of zone refining (see section 2.6) can increase the purity of the sample. Limitations to the sample diameter are set by the surface tension of the material which has to overcome the gravity. The maximum thickness of the liquid layer can be estimated by [25]:

$$t_{\max} = 2.8\sqrt{\frac{\sigma}{\rho g}}, \tag{2.1}$$

where σ is the surface tension of the liquid material, ρ its mass density and $g = 9.81 m/s^2$. In the case of silicon $t_{\max}$ is in the order of 17 mm which is a challenge for large diameter crystals. Most heating methods cannot be focused to such a small layer or are focused to a relative thin surface layer. However, alternative approaches for the heating (e.g. laser heating) as well as electro-magnetically assisted processes can overcome this limit.

2.4 Verneuil method

The Verneuil method is named after Auguste Verneuil who invented this crystal growing technique in 1902. Today the Verneuil method is widely used to produce synthetic gemstones.

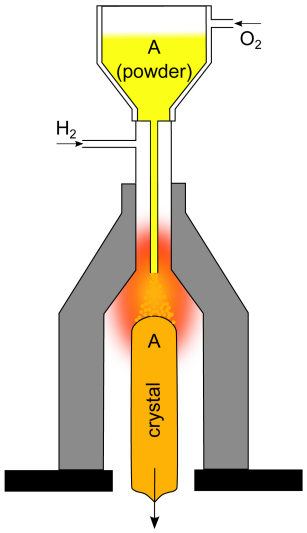

Figure 2.9: Crystal growth after Verneuil.

The raw material is fed into a flame which typically is produced by hydrogen and oxygen to reach high termperatures. The material melts within the flame and is blown onto a seed crystal where crystallisation takes place. The Verneuil method is a crucible-free crystal growing technique that results in crystals of rather small diameters (20...50 mm).

A slightly altered process is used to produce ulta high purity fused silica. Here, high purity silicon tetrachloride ($SiCl_4$) is added to a hydrogen/oxygen flame where it reacts forming high purity silica and hydrochloric gas. This process is known as flame hydrolysis.

2.5 Others

There exist many other crystal growing techniques that focus on different aspects of the crystal (material, purity, orientation, etc.). Many of them are triggered by the need of special single crystals for research and industry. Crystals for non-linear optics or laser crystals are an example that are widely grown by techniques adopted to the specific needs.

Examples of these crystal growing techniques are:

- Crystal growth from solutions,
- pedestal growth of single crystals,
- micro-pulling-down,

where the two last techniques might be of interest for growing crystalline suspension elements for cryogenic applications in GW detectors.

2.6 Zone refining technique

The zone refining technique, which is closely related to the float zone technique, was developed by Pfann et al. [26, 27] in the middle of the 20th century. The aim is to purify already grown single crystals be remelting them in a thin zone and moving the molten zone through the crystal. The zone refining method was the first method that allowed the production of high purity crystals. This triggered detailed studies of electronic properties of semiconductors where impurity concentrations of the order of $10^{-2}...10^{-6}$ ppm can lead to measurable effects.

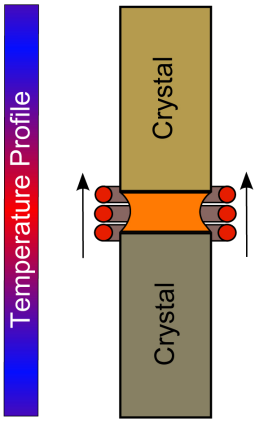

Figure 2.10: Zone refining method used to purify single crystals. The upper crystal is the raw single crystal which contains a large quantity of impurities.

The basic physical process behind the zone refining is the fact the the solubility of the impurity material is different in the solid crystal compared to the melt. The ratio

$$\kappa = \frac{c_{\text{solid}}}{c_{\text{liquid}}} \tag{2.2}$$

is a measure how good an impurity is dissolved in the melt. κ is called the segregation coefficient and is given in tab. 2.1 for different materials. This coefficient is typically < 1 indicating that the impurity gets easier dissolved in the melt. A thin part of the crystal (see section 2.3.5) is heated and transfered into the liquid state. The liquid section is slowly moved through the crystal. All impurities having $\kappa < 1$ will become enriched in the liquid phase and are transferred to one end of the crystal. Multiple subsequent

Table 2.1: Examples of the segregation coefficient κ of different impurities in silicon [28].

impurity	κ	impurity	κ
Al	0.002	O	0.25 - 1.25
As	0.3	P	0.35
B	0.8	Sn	0.016
C	0.07	Zn	10^{-5}
Cu	4×10^{-4}		

refining processes can dramatically increase the purity of the sample. A purification ratio of about 10^6 can be achieved for different impurities using typically 10 repeated refining steps.

3 Mechanical loss and its measurement

The following chapter gives a short overview about the field of anelasticity as the origin of mechanical loss in solids. After that the measuring and analysis procedures needed to study intrinsic losses of solids are reviewed.

3.1 Anelastic behavior of solids

The origin of mechanical dissipation can be found in the elastic properties of a material. It turns out that especially an anelastic behavior causes mechanical loss. For that reason in this section an overview on the treatment of anelasticity is presented.

The well-known basis for an investigation of anelasticity is formed by the pure elasticity as initially described by Hooke's law. He stated a strict proportionality between mechanical stresses σ and mechanical strains u in a purely elastic solid. In the simplest one-dimensional case this statement reads

$$\sigma = Y u \ , \tag{3.1}$$

where Y represents the constant of proportionality and is called Young's modulus. The generalization to a three-dimensional treatment leads to the introduction of stress and strain tensors showing a rank of two. Also Young's modulus is generalized to a tensor of fourth rank, necessarily.

Inherent to this model is the absent of time. For this reason it describes an instantaneous reaction of elastic materials. Thus, the reaction of a solid to an applied time-dependent stress leads to a mechanical strain fully matching the temporal behavior of the applied stress. It is clear that this assumption will break down when acoustic waves travel through the solid. Such a non-static behavior sets in at the frequency of the first mechanical eigenmodes of the solid. The latter depends on the material properties and the sample dimensions and is typically in the range from some Hz for macroscopic vibrating reeds till several MHz for micromechanical resonators.

But even at low frequency, i. e. in the static regime of Young's theory, experiments have shown a deviation from pure elasticity. If e. g. an external stress is applied to a solid as a step function then Young's model predicts the same temporal behavior also for the observed strain. In the experiment such an instantaneous contribution is observed. But also an anelastic creep is superimposed to it leading to a slow relaxation towards the equilibrium strain. This behavior is demonstrated in fig. 3.1

Similar considerations hold for experiments applying a step-wise strain and measuring the stress over time. An empirical model to explain the results of both experiments can be found by the combination of springs and dashpots. Their combination to the network

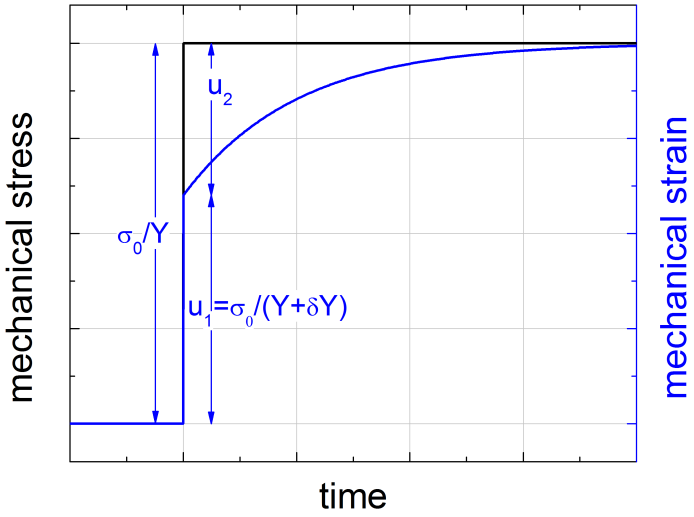

Figure 3.1: Anelasticity in a creep experiment. The application of a mechanical stress σ_0 leads to an instantaneous strain u_1 and a creep contribution u_2 relaxing to the equilibrium strain. The latter represents a typical anelastic effect.

presented in fig. 3.2 forms the basis for the model of the standard anelastic solid (SAS). The working principle shall be illustrated by an applied strain. There the left spring just gives a constant stress. The right path consisting of the dashpot and the spring shows a different reaction. Here due to the fast application of strain the dashpot appears to be extremely stiff and nearly all the strain is applied to the spring. This results in an additional stress contribution via δY. Later the dashpot relaxes and in the end takes the whole external strain. Then no stress is added by the right part leading to the discussed creeping behavior.

Further the response of an SAS to harmonic vibrations is to be investigated. For that purpose a quantitative analysis of the model system is carried out using the constitutive

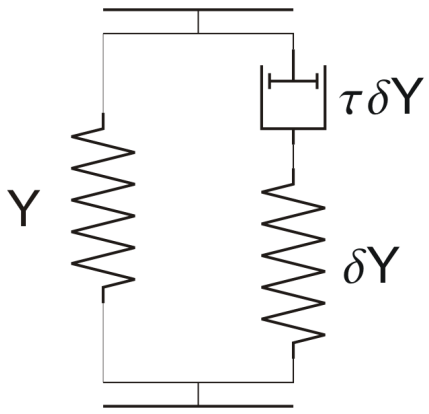

Figure 3.2: Model network for the standard anelastic solid.

equations of the spring and the dashpot as

$$\sigma = Yu \ , \qquad\qquad \sigma = \eta\dot{u} = i\omega\eta u \ , \tag{3.2}$$

respectively. With $\eta = \tau\delta Y$ the elastic behavior of the SAS is found in an effective elastic constant as

$$Y_{SAS} = Y + \delta Y \frac{\omega^2\tau^2}{1+\omega^2\tau^2} + i\delta Y \frac{\omega\tau}{1+\omega^2\tau^2} \ . \tag{3.3}$$

Here one obtains the unrelaxed modulus $Y_{SAS}(\omega \to \infty) = Y + \delta Y$ and the relaxed modulus $Y_{SAS}(\omega \to 0) = Y$. These values also determine the strains u_1 and u_2 in the creep experiments of fig. 3.2.

The imaginary component of Y_{SAS} introduces a phase lag between stress and strain. Consequently, this phase lag leads to a mechanical energy loss that can be calculated as

$$dE = \sigma du = \sigma\dot{u}dt \tag{3.4}$$

The integration over one period T leads to an energy change

$$\Delta E = -\pi\hat{Y}\hat{u}^2 \sin\varphi \ , \tag{3.5}$$

where $\hat{Y}$ and φ have been defined via $Y_{SAS} = \hat{Y}\exp(\mathrm{i}\,\varphi)$ and $\hat{u}$ represents the strain amplitude. Then the mechanical loss is accessible by its definition as

$$\phi = \frac{1}{2\pi}\frac{\Delta E}{E_{tot}} \ , \tag{3.6}$$

with the total elastic energy $E_{tot} = 1/2\hat{Y}\hat{u}^2$ resulting in

$$\phi = \sin\varphi \ . \tag{3.7}$$

For the approximation of small mechanical losses, i. e. $\delta Y \ll Y$ one finds

$$\phi = \frac{\delta Y}{Y}\frac{\omega\tau}{1+\omega^2\tau^2} \ , \tag{3.8}$$

which is known as a Debye peak in the literature (see e.g. [29]). The prefactor $\delta Y/Y$ is typically known as the relaxation strength of a loss mechanism.

3.2 Experimental scheme of mechanical loss measurements

The mechanical loss of solids can be probed in different ways. The two main experimental approaches are acoustic attenuation spectroscopy based on ultrasonic pulses and the mechanical ring down spectroscopy. The former technique probes the mechanical loss with high frequency pulses typically above 10 MHz. The mechanical ring down spectroscopy uses the intrinsic modes of the test samples that are typically in the acoustic band or

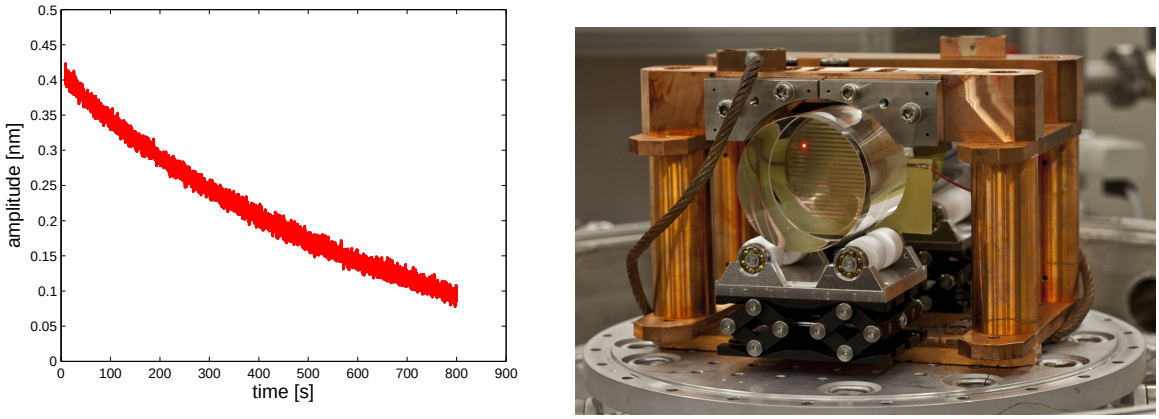

(a) (b)

Figure 3.3: (a) - Free decaying resonant mode of a sapphire test mass (dia. 76 mm, thickness 24 mm, orientation: c-axis) at 36 kHz and 15 K. (b) - Setup for cryogenic mechanical loss spectroscopy used by the group in Jena.

slightly above. The typical operational frequency - and thus the frequency range of interest - for gravitational wave detectors will be between 1 Hz and a few kHz. For this reason mechanical ring down spectroscopy is prefered in order to study the intrinsic losses of optical components.

The object under investigation - typically a cylindrical bulk material or a thin flexure - are excited by means of an electrical comb structure that is fed by an AC signal from a high voltage amplifier. The frequency is tuned until it is in resonance with the intrinsic mode of the sample at f_0. After a certain amplitude, typically in the range from 1 to 100 nm, is reached the excitation is switched off and the subsequent free ring down is recorded (see fig. 3.3).

The characteristic ring down time τ is the duration of the amplitude to decay from the maximum to 37% (1/e) of its initial value. This ring down time is related to the mechanical Q-factor of the resonance by means of

$$Q = \pi f_0 \tau. \tag{3.9}$$

The amplitude is recorded by means of a capacitive, inductive or optical read-out. A preferable method is the use of a Michelson interferometer where one end mirror is formed by the sample under investigation (see fig. 3.4(a)).

The mechanical Q-factor of the resonance is related to the intrinsic mechanical loss ϕ in the case of $Q \gg 1$ (small damping):

$$\phi = 1/Q \tag{3.10}$$

and thus the mechanical loss can be determined by Q-factor measurements at the resonances of the test sample.

The mechanical loss spectroscopy described above always measures the total mechanical loss of the sample that can be summarised as:

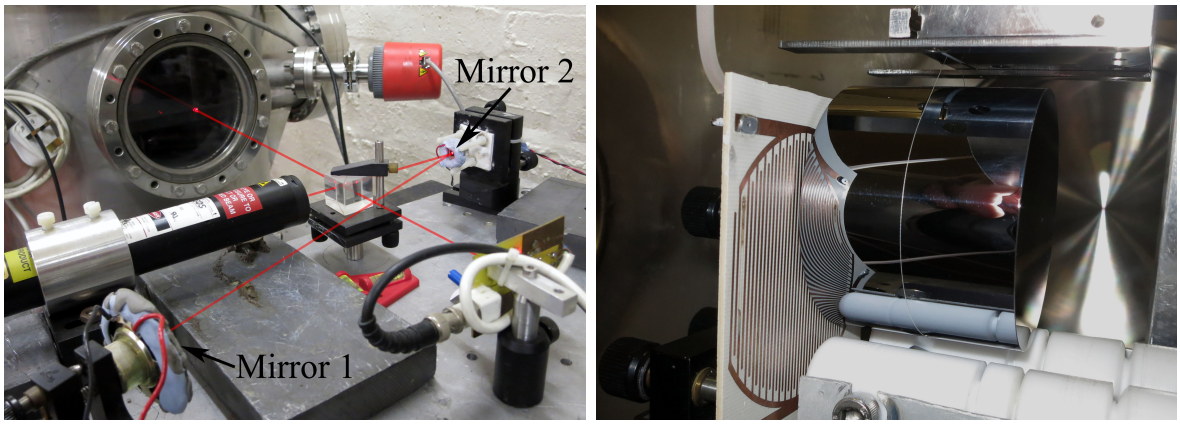

(a) (b)

Figure 3.4: (a) Optical read-out based on a Michelson interferometer used at the Glasgow measuring setup to investigate mechanical losses of bulk samples. (b) Suspended test mass using a silk thread for mechanical loss measurements.

$$\phi_{\text{total}} = \phi_{\text{internal}} + \phi_{\text{external}} \tag{3.11}$$

where ϕ_{internal} is the internal loss of the material (the value that is to be investigated) and ϕ_{external} is the sum of all external damping mechanisms, e.g. gas damping, friction between sample and suspension, recoil losses, etc. All external damping sources have to be very well known and reduced below the level of the intrinsic contribution by means of sophisticated experimental techniques [1, 30, 31].

However, even if the extrinsic losses can be excluded the mechanical spectroscopy only reveals the sum of all inrinsic losses. Thus, it is necessary to change the sample material, the sample geometry and its treatment in repeated measurements to increase or decrease special intrinsic losses to understand their composition. Typically, the sum of the intrinsic losses is dominated by a combination of thermo-elastic, phonon-phonon and impurity induced damping. The current state of knowledge about the different loss mechanisms is summarised in chapter 4.

3.3 Numerical calculation of mechanical mode shapes

A precise knowledge of the mode shape is important in order to be able to minimise external losses and to understand well known intrinsic mechanical loss processes. As samples with an arbitrary geometry and crystal symmetry should be analyzed a numerical calculation is the most convenient approach. Actually, the analysis of mechanical resonances is a standard task for commercial FE packages. In our work we thus use ANSYS [32] and COMSOL [33] for this purpose. Such an analysis demands the elasticity tensor and the density of the material and yields the mode frequencies as well as the mode shapes and energy distribution in the sample. Two modes are exemplarily shown in fig. 3.5.

Even if there are small systematic deviations in the calculated mode frequencies this tool allows a reliable identification of the excited mode at least at low frequencies. This

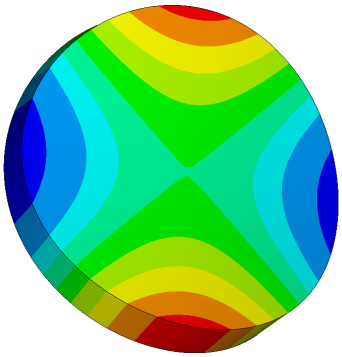

(a) $f_{FE} = 11\,370\,\text{Hz}$, $f_m = 11\,670\,\text{Hz}$

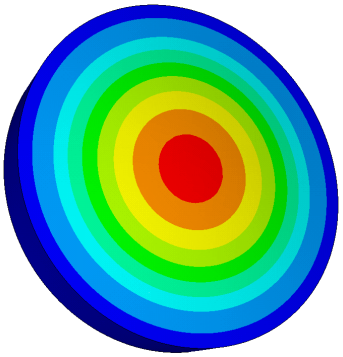

(b) $f_{FE} = 16\,330\,\text{Hz}$, $f_m = 16\,890\,\text{Hz}$

Figure 3.5: Selected mode shapes and calculated mode frequencies f_{FE} of a cylindrical quartz sample in z-cut (diam. 76.2 mm, height 12 mm). The measured frequencies f_m are about 3% higher than the calculated values. This could be explained by slight variations in the elastic constants or the sample geometry.

represents the starting point for any quantitative loss analysis as e.g. in the case of thermoelastic damping or for the investigation of lossy energy contributions by means of the elastic dipole (see Sec. 4.6). Further also qualitative conclusions can be drawn as for the damping due to the suspension. Finally the numerical calculation provides a valuable tool in the measurement process. As the resonances in high Q-materials are very sharp an excitation of these resonances is only effective in a small frequency regime. If the resonant frequency is unknown a fine sweep of the excitational frequency is necessary which costs a lot of time. Thus the numerical results guide the experiment for a faster identification and excitation of elastic modes.

4 Mechanical loss mechanisms in solids

The model of anelastic relaxation presented in the previous chapter represents a purely empiric theory. Thus, in the mentioned model there is no possibility to identify processes causing the phase shift between the stress and strain and consequently a dissipation. In this chapter the underlying effects leading to a phase lag will be identified and be explained physically. This knowledge is crucial for a reliable loss minimization. It therefore preceeds any systematic sensitivity increase in gravitational wave detectors or other highly sensitive metrological setups.

4.1 Overview

Microscopical explanations for mechanical dissipation can be classified into two groups. The first group of mechanisms are inherent even to perfect crystalline materials without defects. Consequently, they mark main restrictions as they cannot be reduced to an arbitrary amount by adjusting the purity. These processes are called to be intrinsic. Thermo-elastic, phonon-phonon and electron-phonon damping can be found among them. A second group is related to defects in the material. Typically the surface and point defects are prominent examples for defects in crystals. Both mechanisms thus trigger mechanical loss processes. Processes in this second group are called to be extrinsic and in principal can be totally omitted by using an inifnitely large crystal with no impurities.

4.2 Thermo-elastic damping

Thermo-elastic damping (TED) is a well investigated loss mechanism. Since the first explanation by Zener in 1937 [34] it has been widely investigated not only as a noise process in gravitational wave detectors but also as the limiting factor for mechanical resonators in the micrometer scale and as a foundation to build effective damping elements. The main principle of thermo-elastic damping is explained in the following. Nearly any deformation of a mechanical sample will cause a volume dilatation in the sample too. With respect to the inverse effect of thermal expansion this volume dilatation will introduce heat into the sample and lead to local temperature changes. Due to Fourier's law a heat flow will set in heading to countervail the temperature gradients. This heat flow increases the entropy of the system and thus dissipates energy.

Another possible explanation considers thermal strain fields on the applied stress. Here the adiabatic deformation only leads to a strain contribution in phase to the applied stress. Due to the heat exchange additional thermal strains will change this behaviour.

As the heat flow marks no instant process, i. e. it takes time to transport thermal energy, it introduces a phase shift between the thermal strains and the stresses. In analogy to the standard anelastic solid this phase shift causes mechanical dissipation.

Zener's original work covers the case of a rectangular beam under pure bending. It gives a thermo-elastic loss of

$$\phi_{TE} = \frac{Y\alpha^2 T}{\rho C}\frac{\omega\tau}{1+\omega^2\tau^2} \ , \tag{4.1}$$

$$\tau = \left(\frac{h}{\pi}\right)^2 \frac{\rho C}{\kappa} \ . \tag{4.2}$$

Here the loss amplitude is affected by Young's modulus Y, the coefficient of thermal expansion α, the temperature T and the specific heat per volume ρC. Further the characteristic time for the heat flow τ is determined by the height h of the beam and the thermal conductivity κ. In a second paper Zener applied his calculation to a circular beam section [35]. There a modification for τ is necessary as follows

$$\tau = \frac{R^2}{2\pi\, 0.539}\frac{\rho C}{\kappa} \ . \tag{4.3}$$

Here R represents the radius of the beam. In 2000 Zener's theory has been refined by Lifshitz and Roukes [36].

The presented load case of a beam under pure bending is especially interesting for the noise analysis of GWD's. There the suspension fibers can be identified as the beam elements and their mechanical loss mainly determines the thermal noise of the suspension structure. In the field of mechanical loss measurements Zener's theory can be applied to cantilever samples operated at bending modes. They typically possess a small thickness compared to the other dimensions.

A model to calculate TED for arbitrary three-dimensional samples, e. g. cylinders, demands numerical means. At first the elastic modeshape has to be determined. From that a second, thermal analysis has to be performed with thermal loads derived by the first analysis. Finally with the help of the temperature field in the sample the heat flows can be integrated to obtain a value for the dissipated energy. The basis for the thermal calculation can be found in the following relation for the entropy density

$$s = \alpha_{ij}\sigma_{ij} + \rho C_p \frac{T - T_0}{T} \ , \tag{4.4}$$

where α represents the tensor of thermal expansion, C_p the specific heat at constant pressure and T_0 the ambient temperature. Typically, the temperature fluctuations $T - T_0$ remain small compared to the ambient temperature T_0. Thus, the temperature term in eq. (4.4) can be replaced by its first order contribution $(T - T_0)/T_0$ yielding the same expression as given in [37].

To derive an equation for the temperature field we start at the conservation of thermal energy. Here the introduced heat density q has to be transported by a heat flux $\vec{k}$ resulting in

$$\frac{\partial}{\partial t} q + \mathrm{div}\vec{k} = 0 \ . \tag{4.5}$$

At this point no external heat sources are considered, which represents the conditions for TED. In the next step $\vec{k}$ is replaced by Fourier's law ($\vec{k} = (-\kappa_{ij})\nabla T$) and the heat dq by Tds. Inserting the entropy density given in eq. (4.4) yields

$$\alpha_{ij} T \frac{\partial}{\partial t}\sigma_{ij} + \rho C_p \frac{\partial}{\partial t} T - \kappa_{ij} \frac{\partial^2}{\partial x_i \partial x_j} T = 0 \ . \tag{4.6}$$

With a slight rearrangement and a further application of the approximation of small temperature fluctuations ($T \approx T_0$) we arrive at

$$\rho C_p \frac{\partial}{\partial t} T - \kappa_{ij} \frac{\partial^2}{\partial x_i \partial x_j} T = -\alpha_{ij} T_0 \frac{\partial}{\partial t}\sigma_{ij} \ . \tag{4.7}$$

Notice that here the Einstein convention has to be used, i. e. one has to implicitly sum over indices that occur more than once.

The structure of the above equation coincides with a simple heat equation. In this analogy the right hand side of the equation represents heat sources originating from the thermoelastic effect. They are caused by the applied stresses σ_{ij}. Consequently, the results of the elastic mode analysis, which is a standard task in FE codes, has to be inserted into the heat conduction problem via σ_{ij}. With that eq. (4.7) has to be solved for the resulting temperature field.

Then the amount of energy dissipation can be calculated by an integration of the heat flows or the work done by the thermal strains against the stress fields (see Refs. [38–40]). Note that both approaches only produce the same results globally, i. e. for an integration over the whole structure. Locally both results may significantly differ from each other. To obtain a physically correct result for a locally resolved energy dissipation the approach with thermal strains has to be used.

Exemplariliy the numerical computation of TED is illustrated on a cylindrical silicon sample. The mode shapes of the anisotropic substrate have been investigated using a finite element analysis. Starting from these results a thermal analysis revealed the level of TED. The amount of heat flows in the sample and with it the level of TED is heavily dependend on the respective mode shape. This dependence is presented for three modes in fig. 4.1. There a spread of two orders of magnitude is visible. In the loss calculation a minimum of TE damping is clearly visible at 120 K due to the vanishing coefficient of thermal expansion.

Since thermoelastic damping is inherent to microstructures the loss spectrum of a vibrating reed (cantilever) is presented in fig. 4.2. There the loss behavior at temperatures above 150 K is clearly dominated by thermo-elastic damping. The loss spectrum shows a dip around 120 K again reflecting the vanishing coefficient of thermal expansion at that temperature. Nevertheless, other loss mechanisms lead to a finite measure of loss at that point. For lower temperatures the thermo-elastic loss becomes significant again. Below 50 K its influence ceases and other loss processes dominate the measured loss. In the case of cantilevers the surface is a strong candidate to contribute significantly to the low temperature loss.

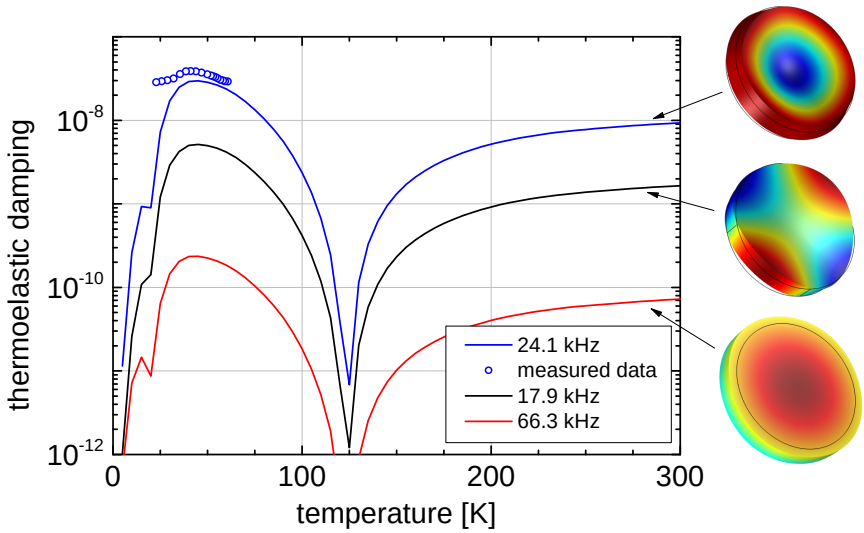

Figure 4.1: Numerical results of TED for a cylindrical silicon sample (diam. 76.2 mm, height 12 mm). The cylindrical axis is oriented along the crystalline ⟨100⟩ direction. Further, the mode shapes and the frequencies of the presented resonances are given. The mode plots show a deformation along the cylindrical axis. Selected data from a loss measurement confirm the existence of the predicted TE loss peak for the 24 kHz sample showing the highest TE loss.

4.3 Phonon-Phonon damping

Another intrinsic loss mechanism can be found in the interaction between phonons. This process was discovered and described in connection to the classical attenuation measurements of acoustic pulses in solids. In an intuitive picture the acoustic phonons that form the acoustic pulse interact with thermal phonons excited in the solid and are scattered. Such a collision is illustrated in fig. 4.3. Consequently, the collision removes energy from the acoustic wave and represents an attenuation process.

In 1937 Landau and Rumer were the first to present a theory based on the picture above [41]. Their theory is based on individual collisions between phonons. This assumption of individual collisions is only valid if the phonon lifetime τ is large compared to their oscillation period $2\pi/\Omega$ ($\Omega\tau \gg 1$). Typically, the thermal motion of the lattice atoms produces irregularities in the lattice. Due to this additional source of scattering this thermal motion mainly determines the phonon lifetime. Consequently, this theory is likely to break down at high temperatures where $\Omega\tau$ falls below 1. There the lattice oscillations are increased and lead to a reduction of the phonon lifetime. As thermal conductivity is dominated by phonons carrying thermal energy, it can be used as a measure for the lifetime. Collisions of phonons will reduce the thermal conductivity. From transport theory it is known, that

$$\kappa = \frac{1}{3}\rho C c_D^2 \tau \ . \tag{4.8}$$

Please note, that only Umklapp-processes affect thermal conductivity. In contrast the

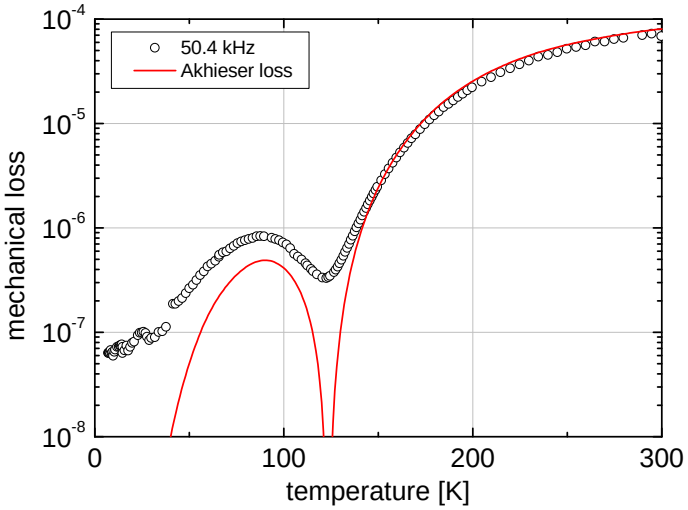

Figure 4.2: Measured mechanical loss of a vibrating reed made of silicon (thickness $\sim$ 110 µm). The line indicates the result of thermo-elastic damping due to the theory of Zener.

phonon lifetime is also reduced by normal processes. Consequently, at low temperatures where mostly normal processes occur the given expressions are likely to largely overestimate τ. Further c_D describes the phonon velocity and an averaged value of

$$\frac{3}{c_D^3} = \frac{1}{c_l^3} + \frac{2}{c_t^3} \ , \tag{4.9}$$

can be calculated from the speed of longitudinal and transversal acoustic waves, c_l and c_t respectively. A rough estimate shows a resulting lifetime in the order of 10^{-12} s at room temperature. Typical resonant frequencies of macroscopic samples for loss measurements are well below 1 MHz. Thus, $\Omega\tau$ is well below 1 and the theory of individual collisions of phonons is not suited to analyze the results of resonant loss measurements.

A second interpretation of phonon-phonon damping was raised by Akhieser in 1939 [42]. In his approach the lifetime of phonons is assumed to be short compared to the phonon frequency ($\Omega\tau \ll 1$). Then collisions effectively take place on scales that are much shorter than the phonon wavelength. Consequently, the acoustic phonon can be treated as a homogeneous background for the thermally excited phonons in the solid. We investigate a volume element that is small compared to the phonon wavelength but large compared to the phonon mean path between two collisions. Within this volume the mechanical strain ϵ applied by the acoustic wave affects the phonon frequency as

$$\Delta\omega_q = \omega_{q0}\gamma_q\epsilon \ , \tag{4.10}$$

with the Grüneisen parameter γ_q. The index q indicates the dependence of this parameter from the momentum of the respective phonon. From this considerations the dissipation process can be understood as follows. Phonons are bosons and thus their population

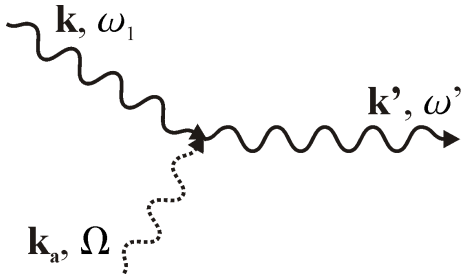

Figure 4.3: Illustration of phonon scattering as an attenuation process in the propagation of acoustic pulses. Here an anihilation process is shown where two incoming phonons form the scattered phonon. In this process the acoustic phonon (dashed) changes its wave vector k_a and its frequency Ω and is removed from the coherent motion of the acoustic wave.

follows a Bose-Einstein-statistic

$$g(\hbar\omega_q) = \frac{1}{\exp\left(\frac{\hbar\omega_q}{k_B T}\right) - 1} \ . \tag{4.11}$$

An unloaded sample will thus exhibit the above equilibrium population of phonons. If now an external strain is applied to the solid due to the Grüneisen parameter the phonon energies are altered. Then the old population does not mark an equilibrium distribution anymore. Due to this fact phonon-phonon collisions set in to bring the phonon population to the new equilibrium. If the mean phonon path length is sufficiently small, this process will run effectively within the investigated volume. In analogy to thermoelastic damping this process can be viewed as a heat flow between different phonon branches. Such a heat flow will produce an entropy increase and lead to dissipation. This view is also plausible by an inspection of eq. (4.11). With a change of ω_q the original population can still be interpreted as an equilibrium population but for a higher temperature. Thus, an external strain changes the temperatures of individual phonon branches and causes a formal heat flow between them.

The reestablishment of the new equlibrium population typically takes a time in the order of the phonon lifetime τ. Here the temporal delay between phonon population and external strain represents the phase lag that causes mechanical loss. A rough model by Bömmel and Dransfeld [43] analyzes the problem of only two groups of phonon branches. The first group shows a vanishing Grüneisen constant while the other branches show the same constant $\gamma \neq 0$. Then the phonon-phonon damping follows

$$\phi_{ph} = \frac{CT\gamma^2}{c_D^2} \frac{\omega\tau}{1 + \omega^2\tau^2} \ , \tag{4.12}$$

where the phonon lifetime is typically taken from the thermal parameters and eq. (4.8). In an application of the above equation to measured data, γ represents the single fitting parameter. The remaining quantities are obtained by the use of material parameters. Further, the validity of the fitted value of γ can be checked on experimental results for the Grüneisen parameter by neutron scattering or third-order elastic constants.

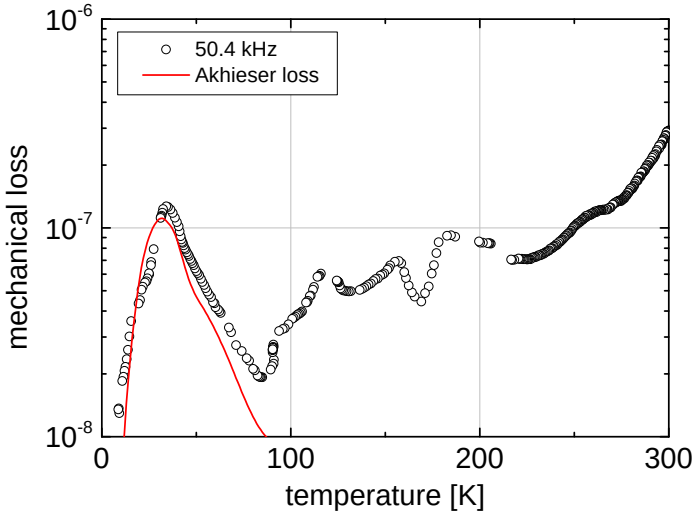

Figure 4.4: Measured mechanical loss of a cylindrical sapphire sample (diam. 76.2 mm, height 24 mm). The line indicates the result of Akhieser's theory for a Grüneisen parameter of $\gamma = 1.4$.

The application of the presented Akhieser theory on the mechanical loss spectrum of a sapphire sample is shown in fig. 4.4. At low temperatures the measured data exhibits a loss peak around 40 K where the loss is increased by the factor 10. Above 100 K a unregular variation of the measured data is visible. Finally above 250 K there is another clear increase of losses for increasing temperatures. Akhieser's theory is able to reproduce the measured data at temperatures below 80 K. The red line in fig. 4.4 represents the results of eq. (4.12) where only γ is left as a free parameter for a fit to the measurement. In our plot a value of $\gamma = 1.4$ leads to the presented result and produces a fair fit to the measured loss spectrum. Further, the presented value is in good agreement with independent measurements of the Grüneisen parameter [44] revealing values between 1 and 3.

4.4 Electron-Phonon damping

A mechanical stress can also lead to an effective force on electrons in the material and thus to an energy transfer to the electronic system. Any dissipation process in the electronic system will then also occur in the mechanical loss spectrum. The interaction process between the mechanical and the electronic system can be understood by a close analogy to Akhieser losses given in Sec. 4.3. Here the external strain leads to a deformation of the electronic dispersion curve. In the simplest model of a free electron gas the dispersion shows a parabolic profile and is radially symmetric. The application of an external strain breaks this symmetry. Then the current electron population marks no equilibrium state any more and a redistribution sets in. This redistribution is closely connected to the time between two collisions of electrons τ_{el}. As this measure also affects the electric

conductivity σ_{el} it can be calculated with this material parameter via

$$\sigma_{el} = \frac{Ne^2\tau_{el}}{m} \ , \tag{4.13}$$

where N is the electron density, e the electronic charge and m the electron mass. Even if the analogy between electron and phonon losses is large one has to bear in mind that electrons exhibit fermionic character while phonons represent bosons. Thus, a difference in both models should occur.

Nevertheless most of the promising candidate materials are semiconductors or insulators. With the largely reduced number of free charge carriers the presented model of the free electron gas looses its justification. In a semiconductor typically only electrons at lowest energy in the conduction band and holes at the highest energy of the valence band determine the electronic behaviour. This is due to the fact, that a thermal excitation of charge carriers happens along an energetical interval of k_BT ($\approx 40\,\mathrm{meV}$ at room temperature) while the fundamental band gap shows an energy around 1 eV. If the maximum of the valence band or the minimum of the conduction band is found at a momentum different than the Γ-point mechanical loss can occur. For now a crystal exhibiting multiple minima in the conduction band is assumed. These minima are called valleys and without an external strain all show the same stress. The equivalent positions can be determined by the symmetry operations of the crystal. An external strain can break this symmetry. Then the energies of the equivalent valleys will split and a thermal redistribution of electrons sets in. This redistribution over an electronic potential barrier leads to a phase lag between the electron population and the external stress. Finally, energy is lost from the strain as an elastic excitation to the electrons and a dissipation is observed. Typically such a process should follow the Debye theory for point defects as given in Sec. 4.6. The deformation potential Ξ represents a key parameter in this process. It describes the change in the valley potential with respect to an external strain ϵ for electronic losses

$$\Delta U = \Xi\epsilon \ . \tag{4.14}$$

In his PhD thesis [45] Lam discussed this process and gave an expression

$$\phi = \frac{\sigma_{el}\Xi^2\omega}{\rho c_s^4 e^2} \ . \tag{4.15}$$

Here the electric conductivity σ_{el}, the mass density ρ, the speed of sound c_s and the electron's charge affect the loss. An estimate for highly doped silicon ($\sigma_{el} = 44\,\mathrm{A\,V^{-1}\,m^{-1}}$) at quite high resonant frequencies ($\omega = 2\pi\,100\,\mathrm{kHz}$) with $\Xi = 5\,\mathrm{eV}$ yields a value of $\phi = 3 \times 10^{-11}$. This value is two orders of magnitude below the lowest reported loss data. Thus, electron damping in silicon turns out to be negligibly small.

Further at low temperatures the number of free charge carriers decreases with respect to the Fermi distribution. This effect additionally reduces the effect of electron damping. The proportionality between carrier density and loss can be found in the electric conductivity σ_{el} in eq. (4.15). For an n-doped semiconductor the electron density in the conduction band reads

$$n_C = \frac{1}{2}n_0 \exp\left(-\frac{E_D}{k_BT}\right)\left[\sqrt{1 + 4\frac{N_D}{n_0}\exp\left(\frac{E_D}{k_BT}\right)} - 1\right] \ . \tag{4.16}$$

Here N_D represents the donor concentration and E_D the energetic distance from the donor level to the conduction band. n_0 is defined as

$$n_0 = \frac{1}{4\pi^3} \left(\frac{2\pi k_B T m_L^*}{\hbar^2} \right)^{3/2} , \tag{4.17}$$

where m_L^* is the effective mass of electrons in the conduction band minimum. Exemplarily the temperature dependence for the electron density is illustrated on the case of silicon doped by phosphor. The results for different doping levels N_D are presented in fig. 4.5. There weakly doped silicon shows a sharp step in the electron density at 40 K. Above this temperature all donors are ionized and the electron density in the conduction band coincides with the doping concentration. This region represents the impurity exhaustion. For an increased doping concentration the step becomes broader. At the extreme doping of $10^{18}\,\mathrm{cm}^{-3}$ even at 300 K not all donors are ionized.

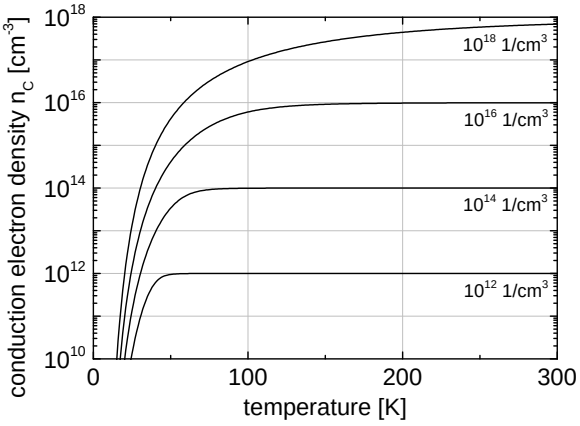

Figure 4.5: Number density of electrons in the conduction band for an n-doped silicon sample (here: phosphor donors). The numerical values indicate the donor concentration N_D. The doping level of phosphor was assumed to be $E_D = 45\,\mathrm{meV}$ below the conduction band minimum.

If the material is piezoelectric another loss mechanism becomes possible. Due to the piezoelectric effect a spatial gradient of the electron potential emerges and leads to an electric force on the electrons. This force leads to a flow of electrons which counteracts the piezoelectric field. Again the finite collision time of electrons causes a phase shift between the electric current and the strain which results in the dissipation of mechanical energy. A microscopic interpretation can also be found in the flow of electrons that causes an entropy increase. This process is in complete analogy to thermoelastic damping and can be treated in the same way.

Another loss mechanism is discussed by Lam [45]. He investigates the interaction of electric dipoles in the material with the electric field caused by the strain. Again a thermally activated reorientation of the dipole is likely which should be described in analogy to point defects. The resulting electrical field reads

$$\vec{E} = \nabla \left(\frac{\Xi \epsilon}{-e} \right) , \tag{4.18}$$

leading to a mechanical loss of

$$\varphi = \frac{\omega^2 \Xi^2}{4\pi e^2 c_s^4 \rho} \epsilon_2 \ . \tag{4.19}$$

Here c_s represents the speed of sound and ϵ_2 the dielectric loss, i. e. the imaginary part of the dielectric constant.

Also impurities are able to induce mechanical loss to semiconductors or even insulators. The underlying loss mechanism is best illustrated at the electronic band structure. An impurity can enter the band gap and form a bounded state exactly as in the typical doping process of semiconductors. Typically, a hole or an electron accompanies the defect. This additional charge carrier itself owns different physically equivalent sites depending on the defect and crystal symmetry. If an external strain splits the energy of such a symmetric defect, an electronic redistribution occurs and results in mechanical loss. This loss process in principle follows the theoretical description of point-induced defects, but emerges from redistributing electrons instead of atoms.

4.5 Surface related damping

An intrinsic defect to all real crystals as a consequence of their finite dimensions is found in the surface. Of course these boundaries break the crystal's translational symmetry and influence also the mechanical loss behavior of real samples. Some examples of possible microscopical situations at the surface are presented in fig. 4.6. Atoms at the surface experience a smaller number of neighbours and typically exhibit unbound electrons which are highly reactive. These electrons known as dangling bonds can flip in the potential of the crystal and cause mechanical loss. Further they can be saturated by impurity atoms from the environment. A special case of this situation can be found in the hydrogenization of this bonds, i. e. a technical saturation of dangling bonds with hydrogen. Then the newly bound atoms will interact with the crystal potential and can cause mechanical loss. Further also dust particles are likely to be bond to the surface.

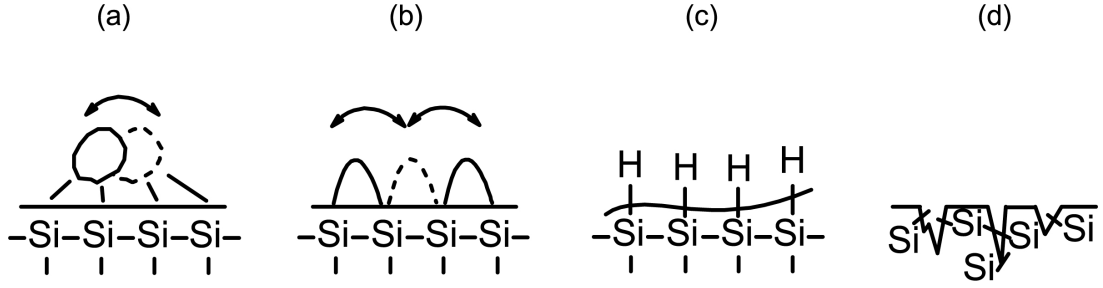

Figure 4.6: Possible microscopical configuration at the surface of crystals, which are likely to cause mechanical loss. (a) - Particles bonded to the surface, (b) - open (dangling) bonds, (c) - terminated surface (here: hydrogen-terminated), (d) - micro-cracks in the surface layer.

Our selection points up the huge variety of possible loss mechanisms at the surface. For this reason the surface can drastically affect the mechanical loss especially of small

structures. Empirical theories have been developed to characterize the surface loss. These theories are based on the assumption of a small boundary layer at the surface as proposed by Gretarsson and Harry [46]. They calculate the energy stored in the surface layer and by a variation of the surface to volume ratio finally estimate the loss contribution of the surface. By this method only a dissipation depth d_s is obtainable. For the most interesting case of the same elastic constants of bulk and surface it gives [46]

$$d_s = \frac{1}{\phi_{bulk}} \int \phi(z) dz \ , \tag{4.20}$$

representing an averaged mean of the spatially dependend surface loss $\phi(z)$. Penn et al. [47] collected existing loss measurements on two types of fused silica. Using the presented model of surface loss and additionally thermoelastic damping they obtain an extremely small value of $\phi = 3 \times 10^{-10}$ as the pure bulk loss for fused silica at 100 Hz. The surface loss is directly proportional to the surface-to-volume-ratio and follows

$$\phi_{surf} = \alpha_s \frac{S}{V} \ . \tag{4.21}$$

In their calculation of the averaged loss parameter α_s a value of 6.5 pm was found for fused silica [47]. The same analysis has been repeated for silicon samples. In their work Nawrodt et al. [48] present a decreased value of $\alpha_s = 0.5$ pm for silicon samples.

4.6 Point-defect induced damping mechanisms

Another well known loss mechanism is caused by the motion of defects in otherwise perfect crystals. Typically, this process is discussed on a point defect in a double well potential. The basics of this loss mechanism is illustrated in fig. 4.7.

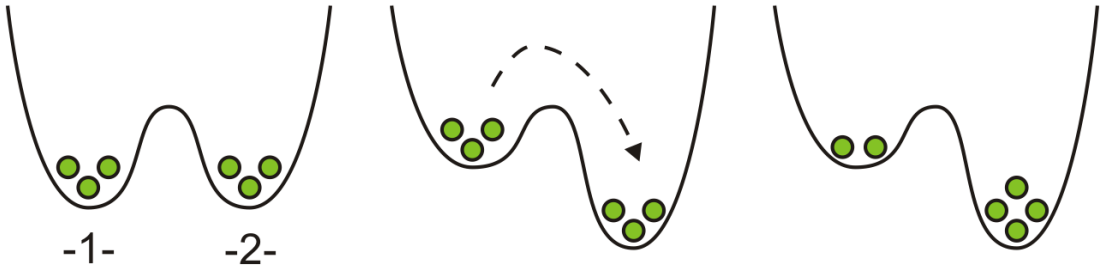

(a) $\epsilon = 0$ (b) $\epsilon \neq 0$ (c) $\epsilon \neq 0$

Figure 4.7: Influence of an external stress on the defect distribution in a double well potential. The diagrams present state energy over a reaction coordinate, e. g. a displacement or a rotation angle. The symmetric double well potential (a) is deformed by an external strain (b). Due to this deformation the equilibrium state is changed and a redistribution driven by thermal energy sets in (c).

At first the energetic potential for a defect within the crystal is shown in fig. 4.7(a) for an unloaded material, i. e. vanishing strain $\epsilon = 0$. In this potential two stable positions

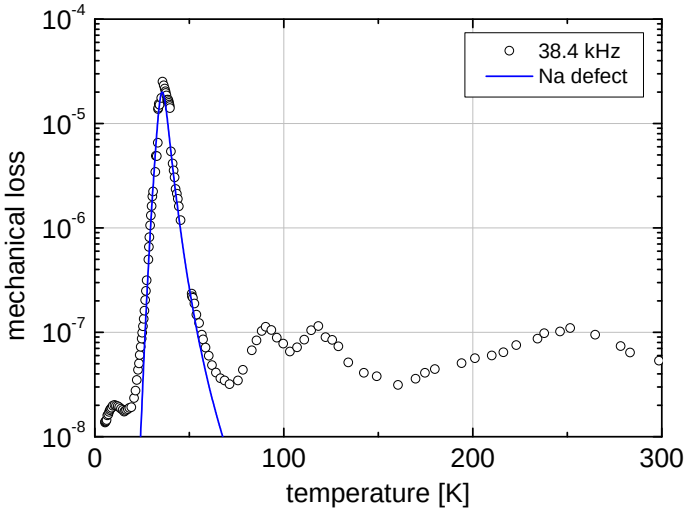

Figure 4.8: Measured mechanical loss of a cylindrical quartz sample in x-cut (diam. 45 mm, height 50 mm). The blue line indicates the mechanical loss of sodium impurities by means of the Debye theory for point defects.

(marked as -1- and -2-) are separated by a potential wall of the height E_a. The thermal energy in the system allows the defects to pass this barrier and thus to establish a dynamic equilibrium population. This equilibrium distribution is theoretically well described by a Maxwell-Boltzmann distribution. Applying an external strain - as in a resonant mechanical loss measurement - can lead to a deformation of the defect potential (see fig. 4.7(a)). If this deformation alters the energy levels of the stable states relative to each other a redistribution of defects will set in. But only defects with an energy above the barrier E_a are allowed to change their state. Thus the typical rate of a redistribution process can be described as

$$\frac{1}{\tau} = \frac{1}{\tau_0} \exp\left(-\frac{E_a}{k_B T}\right) \ , \tag{4.22}$$

where τ_0 is a process dependend constant. Due to the thermally driven redistribution there are more defects in the energetically lower state. To change the defect potential an external strain has to perform work on the defects to change the potential. This represents the microscopical explanation of the mechanical loss introduced by defects. The phenomenological phase lag in this process appears between the applied strain and the defect population. Consequently, for point defects the loss peak follows a Debye law

$$\varphi = \Delta \, \frac{\omega\tau}{1+\omega^2\tau^2} \ , \tag{4.23}$$

with the relaxation strength Δ and τ given above. Together with eq. (4.22) the maximum loss occurs at the condition

$$\omega\tau = \omega\tau_0 \exp\left(\frac{E_a}{k_B T}\right) = 1 \ . \tag{4.24}$$

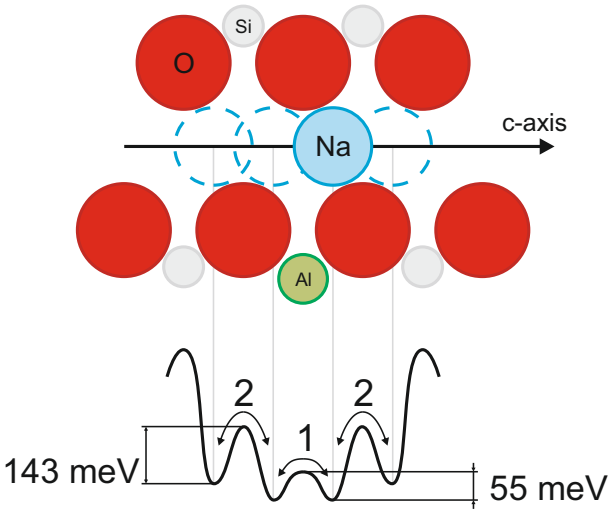

Figure 4.9: Defect potential of sodium in quartz. The potential barrier heights are accessible via loss measurements.

Thus, a plot of $\ln \omega$ on the inverse temperature $1/T_{\max}$ of the maximum loss yields a linear graph

$$\ln \omega = \ln \frac{1}{\tau_0} - \frac{E_a}{k_B} \frac{1}{T_{\max}} \ . \tag{4.25}$$

This so-called Arrhenius plot allows the determination of the activation energy of the defect and its characteristic time constant τ_0.

A prominent example of a defect induced loss mechanism is found in crystalline quartz. There aluminum is incoorporated as an silicon intersitial in the lattice. An alkali atom is necessary to compensate the charge of the defect. Among the alkali elements sodium was identified [49] to show a large dissipation peak around 13 K at frequencies around some 10 kHz. This peak is also visible in the Jena samples. The typical behavior is illustrated in fig. 4.8. Investigating these mechanical loss peaks leads to the defect potential presented in fig. 4.9. There the barrier heights in the sodium potential have been derived from the mechanical loss measurements.

Additionally an Arrhenius plot for the same defect peak but another quartz sample is exemplarily shown in fig. 4.10. The analysis of this diagram yields an activation energy of (59 ± 3) meV and is in good agreement with Martin et al., who reported 57 meV [49].

Not all applied strains will lead to an asymmetric deformation of the defect potential. With respect to the given defect and lattice symmetries one is able to identify strains that only allow a symmetric deformation. As a symmetric deformation does not give rise to any redistribution of defects no loss will be visible for these strain components. Nowick and Heller [50, 51] systematically investigated these symmetry effects in their theory on the elastic dipole. They also present tables where the group theoretical conditions on the existence of mechanical loss is obtainable for arbitrary crystal and defect symmetries.

The concept of the elastic dipole shall be illustrated on the application to mechanical loss in silicon. Mechanical loss spectra in silicon show a peak around 120 K with an activation energy of ca. 170 meV. This peak is often discussed in connection to oxygen

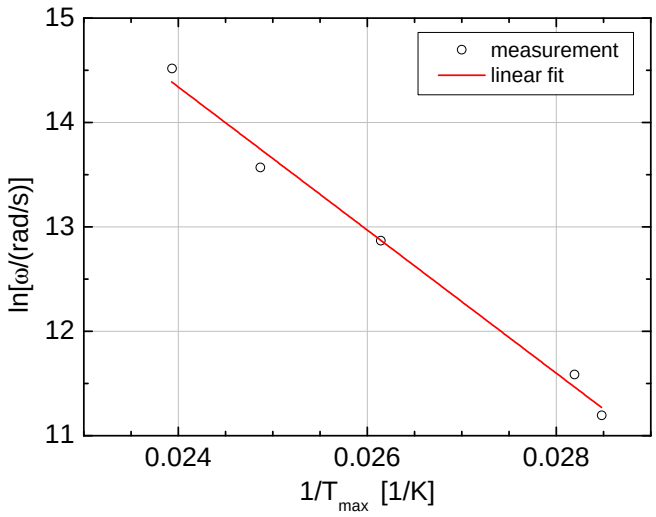

Figure 4.10: Arrhenius plot of the Na defect peak near 50 K for a cylindrical quartz sample in z-cut (diam. 76.2 mm, height 12 mm). The line indicates the linear fit of the measured data and yields an activation energy of (59 ± 3) meV.

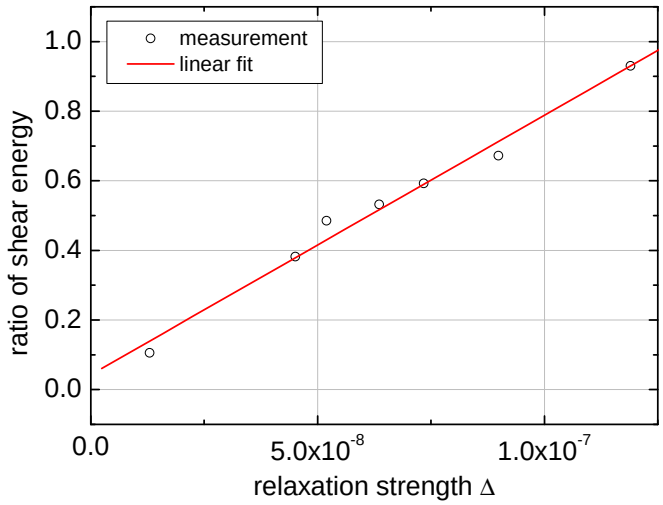

Figure 4.11: Relaxation strength vs. shear energy of the investigated modes for a cylindrical silicon sample (diam. 65 mm, height 70 mm). The linear behavior follows the predictions of the theory for the elastic dipole.

impurities. E. g. Nowick and Heller discuss the trigonal Si-O-Si defect in the cubic silicon lattice in their original work [50]. Due to their theory this constitution should give rise only to a breaking of symmetry for shear components of stress and strain. Consequently, the peak height should scale with the shear energy of the mechanical mode. For this reason the shear energy of measured modes have been calculated numerically by means of FEM. The relative strain energy was then plotted over the relaxation strength Δ taken from the measured spectra for different mechanical modes. The result of this procedure is presented in fig. 4.11. There a linear dependence between relaxation strength Δ and the ratio of shear energy is observed. Even if this result follows the predictions by Nowick and Heller it is no unique proof of the microscopical loss process. Especially the measured activation energy of 170 meV contradicts a reorientation of bonds. As this process should also be responsible for a diffusion of oxygen, the energy scale in diffusion experiments should show the same order. Nevertheless, these experiments [52] yield values in the range of 2.5 eV. Thus, the microscopical origin of the uncerlying mechanical loss process is not understood yet.

Acknowledgement

This work has been performed with the support of the European Commission under the Framework Programme 7 (FP7) "People", project ELiTES (Grant Agreement 295153).

Bibliography

[1] S. Rowan, G. Cagnoli, P. Sneddon, J. Hough, R. Route, E. K. Gustafson, M. M. Fejer, and V. Mitrofanov. Investigation of mechanical loss factors of some candidate materials for the test masses of gravitational wave detectors. *Physics Letters A*, 265(1):5–11, 2000.

[2] M. Punturo, M. Abernathy, F. Acernese, B. Allen, N. Andersson, K. Arun, F. Barone, B. Barr, M. Barsuglia, M. Beker, et al. The Einstein Telescope: a third-generation gravitational wave observatory. *Classical and Quantum Gravity*, 27(19):194002, 2010.

[3] R. Nawrodt, S. Rowan, J. Hough, M. Punturo, F. Ricci, and J.-Y. Vinet. Challenges in thermal noise for 3rd generation of gravitational wave detectors. *General Relativity and Gravitation*, 43(2):593–622, 2011.

[4] S. Hild, M. Abernathy, F. Acernese, P. Amaro-Seoane, N. Andersson, K. Arun, F. Barone, B. Barr, M. Barsuglia, M. Beker, et al. Sensitivity studies for third-generation gravitational wave observatories. *Classical and Quantum Gravity*, 28(9):094013, 2011.

[5] Yu. Levin. Internal thermal noise in the LIGO test masses: A direct approach. *Physical Review D*, 57(2):659, 1998.

[6] S. Rowan, J. Hough, and D. R. M. Crooks. Thermal noise and material issues for gravitational wave detectors. *Physics Letters A*, 347(1):25–32, 2005.

[7] A. A. Chernov. Crystal growth science between the centuries. *Journal of Materials Science: Materials in Electronics*, 12:437–449, 2001.

[8] J. Bohm. The history of crystal growth. *Acta Physica Hungarica*, 57:161–178, 1985.

[9] R. Feigelson. *50 Years Progress in Crystal Growth: A Reprint Collection*. Elsevier Science, 2004.

[10] S. K. Ghandhi. *VLSI Fabrication Principles: Silicon and Gallium Arsenide, 2nd Edition*. Wiley-Interscience, 2 edition, 1994.

[11] R. A. Laudise. Hydrothermal synthesis of crystals. *50 Years Progress In Crystal Growth: A Reprint Collection*, page 185, 2004.

[12] S. Kyropoulos. Ein Verfahren zur Herstellung großer Kristalle. *Zeitschrift für anorganische und allgemeine Chemie*, 154(1):308–313, 1926.

[13] J. Czochralski. Ein neues Verfahren zur Messung der Kristallisationsgeschwindigheit der Metalle. *Z. Phys. Chem.*, 92:219–221, 1918.

[14] J. Evers, P. Klüfers, R. Staudigl, and P. Stallhofer. Czochralskis schöpferischer Fehlgriff: ein Meilenstein auf dem Weg in die Gigabit-Ära. *Angewandte Chemie*, 115(46):5862–5877, 2003.

[15] S. Pizzini. Chemistry and Physics of Defect Interaction in Semiconductors. *Solid State Phenom.*, 85–86:1–66, 2002.

[16] R. C. Newman. Oxygen diffusion and precipitation in Czochralski silicon. *Journal of Physics: Condensed Matter*, 12(25):R335, 2000.

[17] C. Schwarz, D. Heinert, K. Haughian, G. Hofmann, J. Komma, I. W. Martin, P. Murray, S. Rowan, P. Seidel, and R. Nawrodt. Mechanical spectroscopy of silicon as a low loss material for high precision mechanical and optical experiments. *Solid State Phenomena*, 184:443–448, 2012.

[18] E. Artacho, F. Yndurain, B. Pajot, R. Ramirez, C. P. Herrero, L. I. Khirunenko, K. M. Itoh, and E. E. Haller. Interstitial oxygen in germanium and silicon. *Phys. Rev. B*, 56:3820–3833, 1997.

[19] J. Coutinho, R. Jones, P. R. Briddon, and S. Öberg. Oxygen and dioxygen centers in Si and Ge: Density-functional calculations. *Phys. Rev. B*, 62:10824–10840, 2000.

[20] C. C. Lam and D. H. Douglas. Internal friction measurements in Boron-doped single-crystal silicon. *Physics Letters A*, 85(1):41–42, 1981.

[21] F. Schmid and D. Viechnicki. Growth of Sapphire Disks from the Melt by a Gradient Furnace Technique. *Journal of the American Ceramic Society*, 53(9):528–529, 1970.

[22] D. Viechnicki and F. Schmid. Growth of large monocrystals of Al2O3 by a gradient furnace technique. *Journal of Crystal Growth*, 11(3):345 – 347, 1971.

[23] C. P. Khattak and F. Schmid. Growth of the world's largest sapphire crystals. *Journal of Crystal Growth*, 225(2-4):572 – 579, 2001.

[24] D. C. Harris. A Century of Sapphire Crystal Growth. Technical report, DTIC Document, 2004.

[25] C. Weissmantel and C. Hamann. Grundlagen der Festkörperphysik, 1981.

[26] W. G. Pfann. Principles of Zone Melting. *Transactions of the American Institute of Mining and Metallurgical Engineers*, 194:747–753, 1952.

[27] W. G. Pfann. Zone Melting: This technique offers unique advantages in purification and in control of composition in various substances. *Science*, 135(3509):1101–1109, 1962.

[28] R. Hull, editor. *Properties of Crystalline Silicon.* INSPEC, the Institution of Electrical Engineers, London, UK, 1999.

[29] A. S. Nowick and B. S. Berry. *Anelastic relaxation in crystalline solids.* Academic Press, 1972.

[30] D. R. M. Crooks, G. Cagnoli, M. M. Fejer, A. Gretarsson, G. Harry, J. Hough, N. Nakagawa, S. Penn, R. Route, S. Rowan, et al. Experimental measurements of coating mechanical loss factors. *Classical and Quantum Gravity*, 21(5):S1059, 2004.

[31] R. Nawrodt, A. Zimmer, T. Koettig, S. Nietzsche, M. Thürk, W. Vodel, and P. Seidel. High mechanical q-factor measurements on calcium fluoride at cryogenic temperatures. *European Physical Journal-Applied Physics*, 38(1):53–60, 2007.

[32] www.ansys.com.

[33] www.comsol.com.

[34] C. Zener. Internal Friction in Solids: I. Theory of Internal Friction in Reeds. *Physical Review*, 52:230–235, 1937.

[35] C. Zener. Internal Friction of Solids: II.General Theory of Thermoelastic Internal Friction. *Physical Review*, 53:90–99, 1938.

[36] R. Lifshitz and M. L. Roukes. Thermoelastic damping in micro- and nanomechanical systems. *Physical Review B*, 61(8):5600–5609, 2000.

[37] A. N. Norris and D. M. Photiadis. Thermoelastic relaxation in elastic structures, with applications to thin plates. *The Quarterly Journal of Mechanics and Applied Mathematics*, 58(1):143–163, 2004.

[38] J. E. Bishop and V. K. Kinra. Elastothermodynamic damping in laminated composites. *International Journal of Solids and Structures*, 34(9):1075–1092, 1997.

[39] M. M. Fejer, S. Rowan, G. Cagnoli, D. R. M. Crooks, A. Gretarsson, G. M. Harry, J. Hough, S. D. Penn, P. H. Sneddon, and S. P. Vyatchanin. Thermoelastic dissipation in inhomogeneous media: loss measurements and displacement noise in coated test masses for interferometric gravitational wave detectors. *Physical Review D*, 70:082003, 2004.

[40] D. Heinert, A. Grib, K. Haughian, J. Hough, S. Kroker, P. Murray, R. Nawrodt, S. Rowan, C. Schwarz, P. Seidel, and A. Tünnermann. Potential mechanical loss mechanisms in bulk materials for future gravitational wave detectors. *Journal of Physics: Conference Series*, 228:012032, 2010.

[41] L. Landau and G. Rumer. Über Schallabsorption in festen Körpern. *Physikalische Zeitschrift der Sowjetunion*, 11:18–25, 1937.

[42] A. Akhieser. On the absorption of sound in solids. *Journal of Physics (USSR)*, 1(4):277–287, 1939.

[43] H. E. Bömmel and K. Dransfeld. Excitation and Attenuation of Hypersonic Waves in Quartz. *Physical Review*, 117(5):1245–1252, 1960.

[44] S. Hunklinger. *Festkörperphysik*. Oldenbourg Wissenschaftsverlag GmbH, München, Wien, 2007.

[45] C. C. Lam. *Study of internal friction in single crystal silicon.* PhD thesis, University of Rochester, Rochester, New York, 1979.

[46] A. M. Gretarsson and G. M. Harry. Dissipation of mechanical energy in fused silica fibers. *Review of Scientific Instruments*, 70(10):4081–4087, 1999.

[47] S. D. Penn, A. Ageev, D. Busby, G. M. Harry, A. M. Gretarsson, K. Numata, and P. Willems. Frequency and surface dependence of the mechanical loss in fused silica. *Physics Letters A*, 352:3–6, 2006.

[48] R. Nawrodt et al. Investigation of mechanical losses of thin silicon flexures at low temperatures. arXiv:1003.2893v1 [cond-mat.mtrl-sci], 2010.

[49] J. J. Martin. Aluminum-related acoustic loss in AT-cut quartz crystals. *Journal of Applied Physics*, 56(9):2536–2540, 1984.

[50] A. S. Nowick and W. R. Heller. Anelasticity and Stress-induced Ordering of Point Defects in Crystals. *Advances in Physics*, 12(47):251–298, 1963.

[51] A. S. Nowick and W. R. Heller. Dielectric and anelastic relaxation of crystals containing point defects. *Advances in Physics*, 14(54):101–166, 1965.

[52] J. W. Corbett, R. S. McDonald, and G. D. Watkins. The configuration and diffusion of isolated oxygen in silicon and germanium. *J. Phys. Chem. Solids*, 25:873–879, 1964.